

**Controlled alignment of supermoiré lattice in double-aligned graphene
heterostructures**

Junxiong Hu^{1,2†}, Junyou Tan^{2†}, Mohammed M. Al Ezzi^{1,2†}, Udvas Chattopadhyay^{1,2},
Jian Gou¹, Yuntian Zheng¹, Zihao Wang³, Jiayu Chen¹, Reshmi Thottathil¹, Jiangbo
Luo¹, Kenji Watanabe⁴, Takashi Taniguchi⁵, Andrew Thye Shen Wee¹, Shaffique
Adam^{1,2}, Ariando Ariando^{1*}

¹Department of Physics, National University of Singapore, Singapore 117542

²Centre for Advanced 2D Materials and Graphene Research Centre, National
University of Singapore, Singapore 117551

³Department of Materials Science and Engineering, National University of Singapore,
Singapore 117575, Singapore

⁴Research Center for Functional Materials, National Institute for Materials Science,
Tsukuba, Japan

⁵International Center for Materials Nanoarchitectonics, National Institute for
Materials Science, Tsukuba, Japan.

†These authors contributed equally to this work.

*Email: ariando@nus.edu.sg

The supermoiré lattice, built by stacking two moiré patterns, provides a platform for creating flat mini-bands and studying electron correlations. An ultimate challenge in assembling a graphene supermoiré lattice is in the deterministic control of its rotational alignment, which is made highly probabilistic due to the random nature of the edge chirality and crystal symmetry of each component layer. In this work, we present an experimental strategy to overcome this challenge and realize the controlled alignment of double-aligned hBN/graphene/hBN supermoiré lattice, where graphene is precisely aligned with both top hBN and bottom hBN. Remarkably, we find that the crystallographic edge of neighboring graphite can be used to better guide the stacking alignment, as demonstrated by the controlled production of 20 moiré samples with an accuracy better than $\sim 0.2^\circ$. Employing this technique, we are first time to fabricate the perfect double-aligned graphene supermoiré lattice and to observe the sharp resistivity peaks at band filling of 0, -4 and -8 electrons per moiré unit cell. Finally, we extend our technique to other strongly correlated electron systems, such as low-angle twisted bilayer graphene and ABC-stacked trilayer graphene, providing a strategy for flat-band engineering in these moiré materials.

The moiré superlattice, created by stacking van der Waals (vdW) heterostructures with a controlled twist angle¹⁻⁶, enables the engineering of electronic band structures and provides a platform for investigating exotic quantum states, both in the weakly interacting electron systems⁷⁻¹⁰, as well as recently in the strongly correlated electron systems¹¹⁻¹⁷. Particularly, when two moiré superlattices contact and interface together, the overlay of double moiré will create a new structure called supermoiré lattice, strongly modifying the lattice symmetry and electronic band structure¹⁸⁻²². Compared with the single moiré potential, the double moiré potential will further break the lattice symmetry and create isolated flat moiré minibands, providing a strategy for the band flattening effect²³. Recently, evidence of possible correlated states was observed in the double-aligned graphene supermoiré lattice²⁴, which triggered further effort to search for other correlated phenomena, such as superconductivity and ferromagnetic states, as observed in twisted graphene systems²⁵. However, due to the sophisticated stacking and the lack of control of rotational alignment, searching for these correlated phenomena in double-aligned supermoiré lattice remains elusive.

In previous studies of graphene/hexagonal boron nitride (G/hBN) supermoiré lattice, several techniques have been developed to control the rotation alignment, such as in situ rotation mediated by atomic force microscope (AFM) tips and polydimethylsiloxane (PDMS) hemisphere^{20,21}. However, these techniques are restricted by either specialized equipment or complicated sample preparation steps. Consequently, the optical alignment of straight edges is still the most popular and

reliable technique for moiré device fabrication^{8-10,14-19,22-30}. Nevertheless, the conventional optical alignment has two limitations. First, the lack of prior understanding of the crystallographic orientation of graphene or hBN, leading to only a 50% and 25% success rate for alignment of a single and double moiré structure, respectively, because the zigzag (armchair) edge of graphene can be unintentionally aligned to either the zigzag or armchair edge of hBN (**Fig. 1a**). Moreover, the lattice symmetry of hBN layer also obscures the inversion symmetry of the moiré heterostructure^{20,21}, further decreasing the success rate to 12.5% (**Fig. 3b, c**). Second, the optical alignment highly depends on the crystal edge of graphene itself and usually it has a short and non-perfect straight edge. This leads to the error in the determination of principle crystallographic axes (PCA) and decreases the accuracy of alignment. Consequently, a perfect double-aligned sample, where the twist angles between graphene and top/bottom hBN are both close to zero, has not been realized so far (**See Table S2**).

In this work, we overcome the above two limitations and realize the control alignment of double-aligned graphene supermoiré lattice. First, we use a rotation 30° technique to control the alignment of top hBN and graphene (**Fig. 1**), while we use a flip-over technique to control the alignment of top hBN and bottom hBN (**Fig. 3**). Based on these two techniques, we can control the lattice symmetry and tune the graphene band structure. In a high-quality perfect double-aligned device with mobility of $\sim 700,000$ cm²/Vs at 2 K, we observe sharp resistive peaks at band fillings of 0, -4, -8 electrons

per moiré unit cell, consistent with our calculated band structure. Second, we show that the neighboring graphite edge can be used to better guide the alignment, as demonstrated by the controlled production of 20 moiré samples with accuracy better than $\sim 0.2^\circ$, significantly improving the productivity and accuracy. Finally, we extend our alignment technique to other correlated systems, such as low-angle twist bilayer graphene and ABC-stacked trilayer graphene, enabling us to examine moiré potential effects in these strongly correlated electron systems.

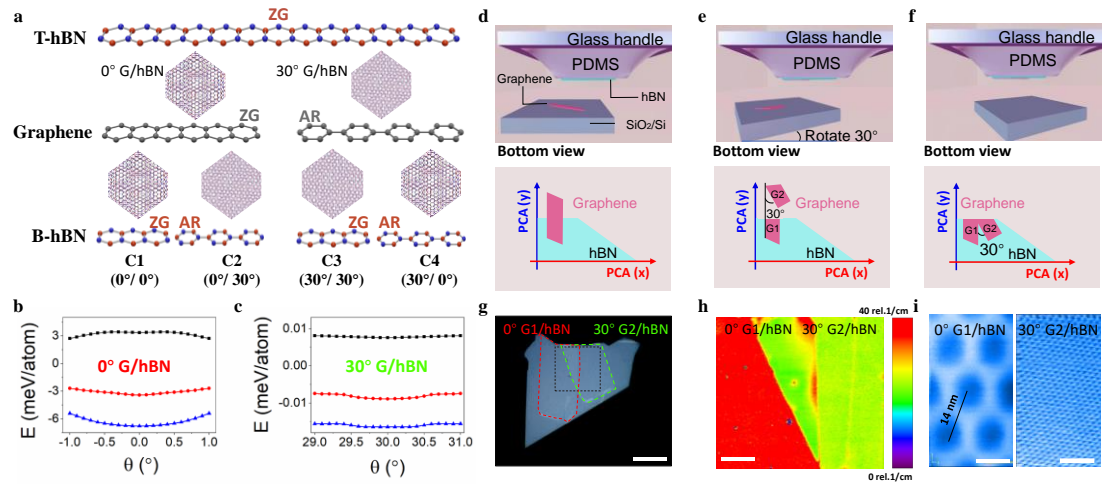


Fig. 1 | Control alignment of T-hBN and graphene by rotating 30° . **a**, Alignment of T-hBN, graphene and B-hBN. The Zigzag (ZG) edge of T-hBN is aligned with the ZG edge or Armchair (AR) edge of graphene and is then aligned with the ZG or AR edge of B-hBN, leading to four possible combinations: C1 ($0^\circ/0^\circ$), C2 ($0^\circ/30^\circ$), C3 ($30^\circ/30^\circ$) and C4 ($30^\circ/0^\circ$). The middle cartoons are two basic moiré patterns of 0° G/hBN and 30° G/hBN. **b,c**, Calculated interaction energies for G/hBN heterostructure around 0° and 30° . Total energy (red circles) contributions from intralayer (elastic energy/blue triangles) and interlayer interactions (adhesive energy/black squares). **d-f**, Side view and bottom view of 30° rotational alignment. **g**, Optical image of G/hBN stack on PDMS stamp. The red dash line profiles the outline of 0° G1/hBN and the green dash line profiles the outline of 30° G2/hBN. Scale bar, $20\ \mu\text{m}$. **h**, Spatial map of the FWHM of 2D-band for the dashed area in **g**. The red color map refers to 0° G1/hBN, while the green color map refers to 30° G2/hBN. Scale bar, $5\ \mu\text{m}$. **i**, The STM topography image of 0° G1/hBN shows $\sim 14\ \text{nm}$ moiré patterns (left, $500\text{mV}, 15\text{pA}$), and the topography image of 30° G2/hBN shows the characteristic of quasicrystal (right, $100\text{mV}, 100\text{pA}$). Scale bar, $10\ \text{nm}$.

First, we study the controlled alignment between top hBN (T-hBN) and graphene. In the optical alignment technique, the G/hBN moiré superlattice is achieved by aligning the PCA between graphene and hBN. Based on the crystallographic structures, they can form two basic moiré patterns: 0° G/hBN and 30° G/hBN (**Fig. 1a, also Fig. S1**). When in the assembly of hBN/graphene/hBN sandwich structure, there are four possible configurations: C1 (ZG/ZG/ZG, $0^\circ/0^\circ$), C2 (ZG/ZG/AR, $0^\circ/30^\circ$), C3 (ZG/AR/ZG, $30^\circ/30^\circ$), C4 (ZG/AR/AR, $30^\circ/0^\circ$) (**Fig. 1a**). All possible combinations lead to 50% single alignment (C2 and C4), 25% double 30° alignment (C3), and 25% double 0° alignment (C1). Our theoretical calculations investigate the adhesive energies of two basic moiré patterns and find that there are two energy minima at 0° and 30° twist angles, indicating these two moiré patterns are energetically stable states (**Fig. 1b, c**). These calculations also suggest that graphene and hBN tend to self-rotate to 0° or 30° when stacked together, depending on the initial states^{31,32}.

Based on these calculations, we develop the so-called “ 30° -rotation technique” to simultaneously obtain these two energy-stable states. The central concept of this technique is illustrated in **Fig. 1d-f**. Instead of directly picking up the whole graphene as in the conventional optical alignment technique, the hBN is aligned partially with a graphene layer (**Fig. 1d**). Thanks to a stronger vdW interaction between graphene and hBN, the graphene layer can be torn into two pieces. The graphene area in contact with hBN can be selectively detached (G1), leaving behind a section of the graphene layer (G2) on the silicon wafer. The critical step in our technique is that the left graphene (G2)

is rotated manually by a twist-angle of 30° (**Fig. 1e**), and G2 is then stacked at another location on the same hBN (**Fig. 1f**). This process results in two G/hBN structures based on the same hBN layer: G1/hBN and G2/hBN (**Fig. 1f**). Since G1 and G2 are 30° rotated to each other, one of them must be 0° aligned with hBN, and the other one must be 30° with hBN (**Fig. S1**). To examine our concept, we investigate the resulting G/hBN structures using optical microscopy, Raman spectroscopy and scanning tunneling microscopy (STM). **Figure 1g** shows the optical image of G/hBN stacks, showing two sections of graphene rotated 30° to each other as indicated by the dashed lines. **Figure 1h** shows the respective FWHM mapping of Raman 2D peaks. The FWHM mapping of the red area is close to 40 cm^{-1} , indicating the 0° rotation between graphene and hBN³³ (**Fig. S2**). While the FWHM mapping of the green area is close to 20 cm^{-1} , indicating the 30° G/hBN. Moreover, the homogeneous distribution mapping indicates the spatially uniform twist angles. To further confirm the twist angles, we also use STM to directly characterize the moiré patterns of G1/hBN and G2/hBN (**Fig. 1i**). The 0° G1/hBN has a clear moiré wavelength of $\sim 14\text{ nm}$ ^{34,35}, while the 30° G2/hBN shows the character of quasicrystal line, which has 12-fold rotational order but lacks translational symmetry^{36,37} (**see also Supplementary Fig. S3**). Moreover, the twist angles are also confirmed by our transport measurements, as discussed later. Therefore, using this 30° -rotation technique, we can always obtain the 0° G/hBN without the need to consider the exact chirality edge of each layer.

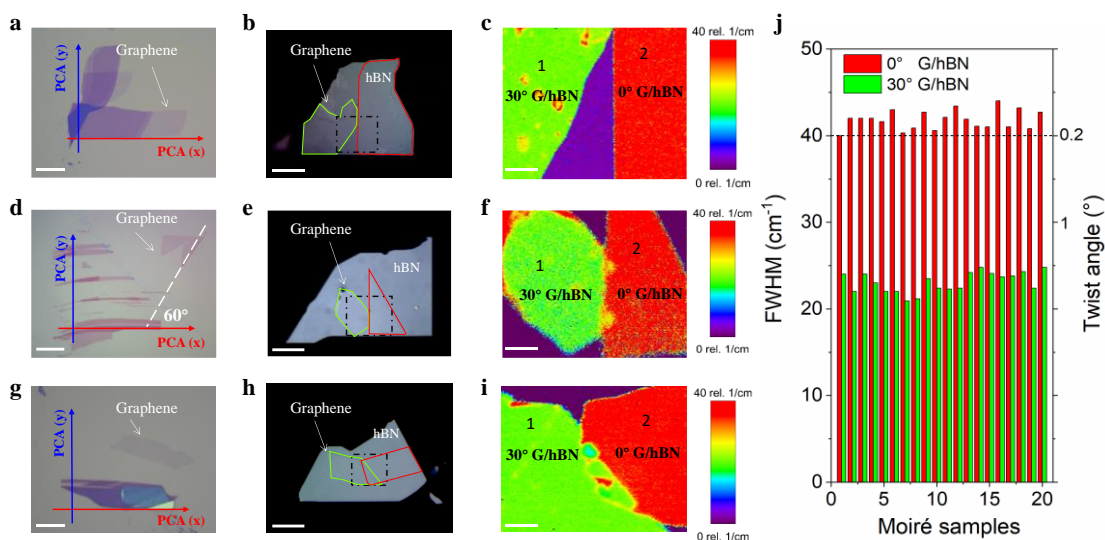


Fig. 2 | Perfect alignment of T-hBN and graphene using the neighboring graphite edge. **a.** Optical image of single-layer graphene connecting with a neighboring graphite edge. **b.** G/hBN stack after alignment using the graphite edge of **a.** **c.** Spatial map of the FWHM of Raman 2D-band for the dashed area in **b.** **d.** single-layer graphene with one edge has 60° with a neighboring graphite edge. **e.** G/hBN stack after alignment using the graphite edge of **d.** **f.** Spatial map of the FWHM of Raman 2D-band for the dashed area in **e.** **g.** single-layer graphene without any connection with an adjacent graphite edge. **h.** G/hBN stack after alignment using the graphite edge of **g.** **i.** Spatial map of the FWHM of Raman 2D-band for the dashed area in **h.** Scale bars, $20\ \mu\text{m}$ (**a**, **d**, **g**); $5\ \mu\text{m}$ (**b**, **e**, **h**); $2\ \mu\text{m}$ (**c**, **f**, **i**). **j.** Histogram of the FWHM of Raman 2D-band and twist angle for 20 moiré samples. The FWHM of $\sim 20\ \text{cm}^{-1}$ (green color) corresponds to 30° G/hBN, and the FWHM of $\sim 40\ \text{cm}^{-1}$ (red color) corresponds to 0° G/hBN.

Even though we can overcome the uncertainty in the edge chirality, there are still two other challenges for optical alignment. First, it is incredibly challenging to identify a single-layer graphene flake with a straight edge, which usually happens in less than 1% from all exfoliated flakes (**Fig. S4**). Second, the single-layer graphene usually is not long and straight enough, decreasing the accuracy in the alignment (**Fig. S5**). To improve productivity and accuracy, we show that the neighboring graphite edge can be better for alignment. The concept is illustrated in **Fig. S6**. **Figure 2** illustrates three typical cases of neighboring graphite edges that can be used for perfect alignment. The first case is that the single-layer graphene has a direct connection with its neighboring

graphite edge (**Fig. 2a**). In this case, the single-layer graphene must share the same PCA with neighboring graphite edges, which means the PCA of graphite can be used for alignment. Our Raman 2D-band mapping confirms one part belongs to 0° G/hBN and the other to 30° G/hBN, as the FWHM of the 2D peaks is 40 and 20 cm^{-1} , respectively (**Fig. 2c**). The second case is that the single-layer graphene has no direct connection with the graphite edge, but one edge of graphene is multiples of 30° with the graphite edge. In this case, the graphene and the neighboring graphite also share the same PCA. Therefore, the PCA of graphite can be used for alignment. Raman 2D-band confirms the alignment since they have 0° G/hBN and the second part has 30° G/hBN (**Fig. 2f**). The third case is that the single-layer graphene neither has any connection nor is multiples of 30° with the neighboring graphite edge (**Fig. 2g**). We show that the PCA of graphite can still be used for alignment if they are close to each other since our Raman spectra show that one part is 0° G/hBN and the second part is 30° G/hBN (**Fig. 2i**).

The best advantage of our technique is that the alignment is not limited by the geometry of graphene itself, and any random shape of single-layer graphene flake can be used for fabricating moiré samples, as long as its neighboring graphite can provide the straight edges (**Fig. S7**). In order to demonstrate the high productivity and accuracy of our strategy, we further fabricate 20 moiré samples, where all the single-layer graphene flakes have a random edge. The histogram shows that the FWHM of all the samples is larger than 40 cm^{-1} , indicating that the accuracy of our alignment is better than $\sim 0.2^\circ$. (**Fig. 2j**, see also **Supplementary Fig. S8**). In comparison, the alignment accuracy

when using a conventional technique is merely $0.5\text{--}1^\circ$ (See the summary in Table S1). Compared with single-layer graphene alignment, we find the PCA of neighboring graphite edges can be better for alignment because the thick graphite edge can have a longer and more straight edge, which can be used to determine a better PCA for alignment. Our results show that a straight graphite edge can always ensure the alignment better than 0.2° , while a non-perfect straight edge or short straight edge ($5\text{--}10\ \mu\text{m}$) will lead to a significant deviation from an ideal alignment ($> 0.5^\circ$) (Fig. S5). Therefore, using the neighboring graphite edge for alignment, we can not only significantly improve the device yields, but also guarantee the high accuracy of alignment.

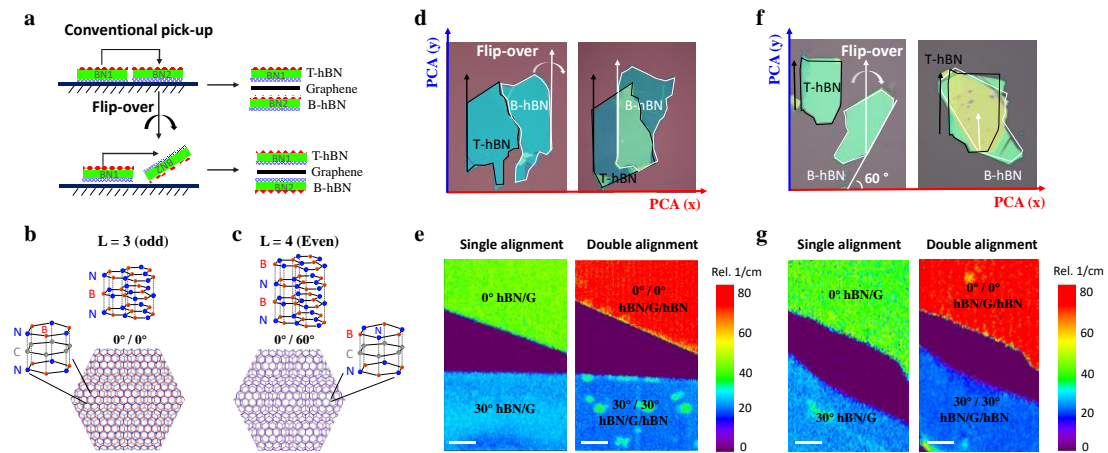


Fig. 3 | Control alignment of T-hBN and B-hBN using the neighboring hBN surface. **a**, Schematics of conventional pick-up and new flip-over technique for double alignment. **b,c**, Schematics of hBN/graphene/hBN heterostructures with odd (**b**) and even (**c**) hBN layers. Lattice models at the high symmetry points of the moiré pattern show the atomic arrangement for each. Purple shading in (**c**) denotes the overlap of boron (red) and nitrogen (blue) in the T-hBN and B-hBN. **d**, Optical images of fractured hBN and alignment of T-hBN and B-hBN using the flip-over technique. The black lines profile the T-hBN, and the red lines profile the B-hBN. **e**, Maps of the FWHM of Raman 2D-band of graphene for the single and double alignment using the hBN in (**d**). **f**, Optical images of two neighboring hBN and one of hBN have 60° with PCA can also be aligned using the flip-over technique. **g**, Maps of the FWHM of Raman 2D-band of graphene for the single and double alignment using the hBN in (**f**). Scale bars, $1\ \mu\text{m}$ (**e**,

g).

Next, we study the control alignment of T-hBN and B-hBN. Because of the uncertain edge chirality of B-hBN, there are again two possible cases when we stack the 0° and 30° T-hBN/G on the B-hBN: C1/C3, if T-hBN and B-hBN have the same edges (**Fig.S9**) and C2/C4, if T-hBN and B-hBN have the different edges (**Fig.S10**). To secure the crystallographic orientation of T-hBN and B-hBN, we can use the same edge of the same hBN for alignment. However, apart from the edge chirality, we also need to consider the lattice symmetry of each hBN layer. As shown in **Fig. 3a**, for the conventional pick-up process, we pick up BN1 and stack it on BN2, so the bottom surface of BN1 is in contact with the top surface of BN2. Depending on the surface symmetry determined by the layer number of hBN, the final stack can be $0^\circ/0^\circ$ or $0^\circ/60^\circ$ (**Fig. 3b, c**). The $0^\circ/0^\circ$ heterostructure has three-fold rotationally symmetric, and the overall structure breaks inversion symmetry, while the $0^\circ/60^\circ$ heterostructure has a six-fold rotationally symmetric and the structure host inversion symmetry. Even though these two structures have the same moiré wavelength, the change of local stack induces a change in the atomic relaxation, consequently leading to totally different bandgaps^{20,23}.

In order to control the alignment of T-hBN and B-hBN, we then develop a “flip-over technique” based on the same crystal edge as well as the same atomic surface. As illustrated in **Fig.3a**, the key step is that BN2 is flipped over that makes the bottom surface of BN2 exposed to the same bottom surface of BN1. In this case, the same lattice symmetry of T-hBN and B-hBN can be guaranteed. **Figure 3d** shows the optical

images of two pieces of hBN that can be regarded as T-hBN and B-hBN, respectively. Combining the 30° rotation and flip-over technique, we can first realize the single alignment and then the double alignment, as demonstrated by the increase in FWHM of Raman 2D-band from $\sim 40 \text{ cm}^{-1}$ (single alignment) to $\sim 70 \text{ cm}^{-1}$ (double alignment) at the same area¹⁹ (**Fig. 3d**, see also **Fig. S11**). In addition, we show that if the two hBN layers are not coming from the same fractured hBN, but their straight edges have the multiples of 30° , which means these two hBN can also share the common PCA (**Fig. 3f**). In this case, we can also realize a perfect double alignment based on the same surface of hBN, as confirmed by the Raman 2D-band shown in the same area (**Fig. 3g**, see also **Supplementary Fig. S11**). Therefore, combining the 30° rotation and flip-over technique, we can overcome the uncertainty in the edge chirality and lattice symmetry during rotation alignment, and realize the 100% success rate for the alignment of the double moiré structure. This is in stark contrast to the conventional technique that can only lead to a 12.5% success rate.

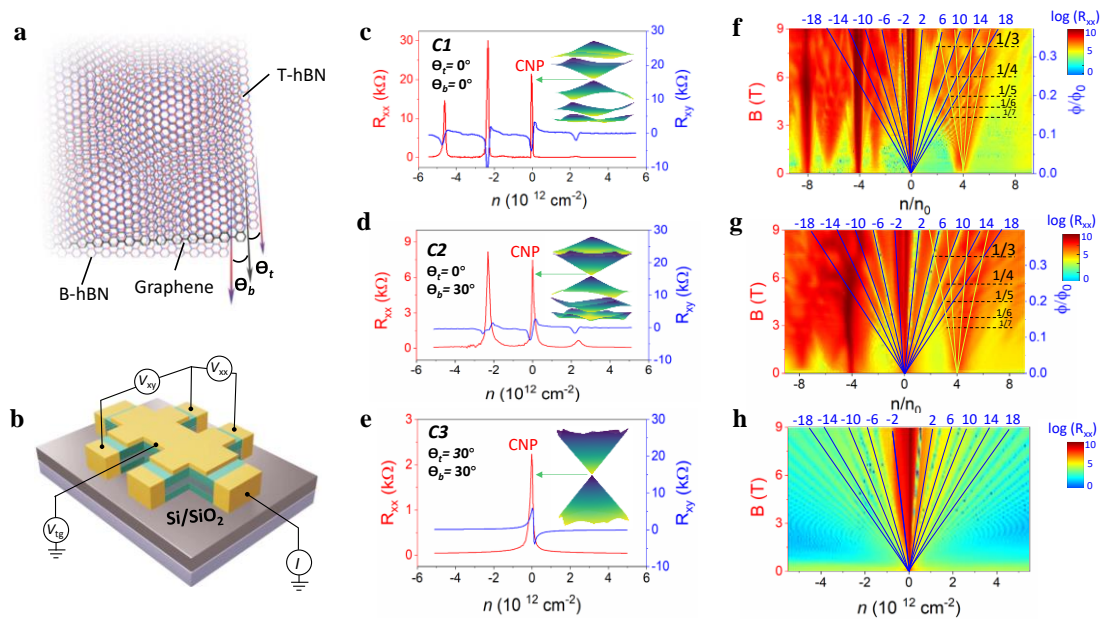


Fig. 4 | Lattice symmetry and band structure tuned by moiré potential in T-hBN/graphene/B-hBN heterostructure. **a**, Art view of the supermoiré lattice with twist angles (θ_t and θ_b) between graphene and T-hBN and B-hBN. **b**, Schematics of the top-gate device with double moiré. Longitudinal resistance (Left axis) and Hall resistance (right axis) with $B = 0.5$ T versus carrier density for **c**, C1 ($0^\circ/0^\circ$), **d**, C2 ($0^\circ/30^\circ$), and **e**, C3 ($30^\circ/30^\circ$). The insets show the corresponding band structures at the K-point. Landau fan diagram of **f**, C1, **g**, C2 and **h**, C3 plotted in magnetic field (left) and corresponding ϕ/ϕ_0 versus n/n_0 . ϕ/ϕ_0 and n/n_0 are the normalized magnetic flux and carrier density, respectively. The top number are the topological index ν to be $\pm 2, \pm 6, \pm 10, \text{etc.}$ $T = 2$ K.

Finally, to reveal the role of moiré potential in the reconstruction of lattice symmetry and band structure, we study the electronic properties of C1-C3 configurations by top-gate devices^{38,39} (**Fig. 4a, b**). For double-aligned C1 ($0^\circ/0^\circ$) device, apart from the neutrality point (CNP), there are also two successive satellite peaks that appear at hole-side, locating at $-n_s$ and $-2n_s$, where $n_s = 2.3 \times 10^{12} \text{ cm}^{-2}$ (**Fig. 4c**). Since n_s is the carrier density required to reach the edge of its first Brillouin zone of a moiré pattern λ by $n_s = \frac{8}{\sqrt{3}\lambda^2}$ ⁸⁻¹⁰, we can calculate the moiré wavelength of C1 of ~ 14 nm, in good agreement with our Raman and STM measurements. Moreover, our band structure calculation (**Inset of Fig. 4c**) shows that the double moiré superlattice significantly splits the hole-sided bands at higher energy into minibands with fully developed gaps at electron fillings of $-n_s, -2n_s$ and $-3n_s$, which is consistent with our observation since these satellite peaks in hole-side bands are more developed than in the electron-side. Moreover, apart from these band filling peaks, we do not observe any extra peaks which may come from the misalignment¹⁸⁻²⁴. Therefore, we can conclude that the C1 sample is a perfect double-aligned sample, where the twist angles between graphene and top/bottom hBN are both close to zero. A similar feature is also observed in another

perfect double-aligned sample (**Fig. S12**). While for single-aligned C2 ($0^\circ/30^\circ$) device, we only observe one satellite peak at hole-side, locating at $-n_s = -2.2 \times 10^{12} \text{ cm}^{-2}$, corresponding to the moiré wavelength of $\sim 14.5 \text{ nm}$ (**Fig. 4d**). The slightly larger moiré periodicity in C2 can be attributed to the strain effect in the heterostructure^{19,24}. The lack of $-2n_s$ peak in C2 suggests that the overlap between the second and third band, as our band structure calculation shows a rather small bandgap (**Inset of Fig. 4d**). When the moiré potential disappears in C3 ($30^\circ/30^\circ$) device, there is only one main Dirac point, consistent with our band structure calculation (**Inset of Fig. 4e**).

When the electrons simultaneously subjected to both a magnetic field and a spatially periodic electrostatic fields, the energy spectrum develops into a Landau fan with a fractal structure known as the Hofstadter butterfly⁸⁻¹⁰, which can be renormalized into a diagram defined by the Diophantine equation: $\frac{n}{n_0} = \nu \frac{\phi}{\phi_0} + s$, where ν is the Hall conductivity in units of a conductance quantum e^2/h , as indicated by black solid lines in **Fig. 4f, g, h**, with topological index ν of $\pm 2, \pm 6, \pm 10, \pm 14, \dots$, and s the index of band filling. $\phi = B \cdot A$ is flux per moiré unit area at magnetic field B , and $\phi_0 = h/e$ is a flux quantum with h being the Planck's constant. **Figure 4f** shows the fracture spectrum of C1 ($0^\circ/0^\circ$) device. The straight minigaps arises at $\frac{\phi}{\phi_0 q}$ ($q = 1, 2, 3, \dots$), resulting in Brown-Zak (BZ) oscillations with the fundamental period field of $B_f = 24.49 \text{ T}$ (ϕ_0/A). Thus, we can calculate the moiré periodicity of D1 of 13.97 nm , which is consistent with the first band filling density at $-n_s = -2.35 \times 10^{12} \text{ cm}^{-2}$. Similarly, the BZ oscillations for C2 device has the $B_f = 23 \text{ T}$ (**Fig. 4g**). We can then calculate the

moiré periodicity of C2 to be 14.417 nm, also consistent with the first band filling $-n_s = -2.2 \times 10^{12} \text{ cm}^{-2}$. When the moiré periods disappear in C3 device, the BZ oscillations also disappear, as there is only the Landau levels spectrum (**Fig. 4h**). These results suggest that the control alignment of moiré patterns, acting as a periodic moiré potential, can tune the lattice symmetry and engineer the band structure.

In conclusion, we develop a generic strategy to overcome the edge chirality and lattice symmetry uncertainty in rotation alignment. Moreover, we show that the neighboring graphite edge can be used for better alignment of the stacking structures, significantly improving the device yield and alignment accuracy. Compared with previous conventional techniques, the current technique is easier and reliable to operate with robust and definite control of alignment. Considering the emerging area of “twistronics”, our technique can be beneficial for much effort in this area in many laboratories. For example, our strategy can also be applied to the family of transition metal dichalcogenide (TMD) semiconductors^{3,4} such as WSe₂/WS₂ moiré superlattice, where a prior measurement of edge chirality in each crystal is necessary before alignment⁴⁰⁻⁴³. To show the universality of our technique, we also extend our technique to other correlated systems, like low-angle twisted bilayer graphene (**Supplementary Fig. S13**) and ABC-stacked trilayer graphene (**Supplementary Fig. S14**). We believe our technique can help effort in exploring the physics of strong electronic correlations and non-trivial band topology in these moiré materials.

References

1. Andrei, E. Y., MacDonald, A. H. Graphene bilayers with a twist. *Nat. Mater.* **19**, 1265–1275 (2020).
2. Andrei, E.Y. et al. The marvels of moiré materials. *Nat. Rev. Mater.* **6**, 201–206 (2021).
3. Mak, K.F., Shan, J. Semiconductor moiré materials. *Nat. Nanotechnol.* **17**, 686–695 (2022).
4. Huang, D. et al. Excitons in semiconductor moiré superlattices. *Nat. Nanotechnol.* **17**, 227–238 (2022).
5. Xie, H. et al. Twist engineering of the two-dimensional magnetism in double bilayer chromium triiodide homostructures. *Nat. Phys.* **18**, 30–36 (2022).
6. Zhao, S. Y. F. et al. Emergent interfacial superconductivity between twisted cuprate superconductors. Preprint at <https://doi.org/10.48550/arXiv.2108.13455> (2021).
7. Yankowitz, M. et al. van der Waals heterostructures combining graphene and hexagonal boron nitride. *Nat Rev Phys* **1**, 112–125 (2019).
8. Ponomarenko, L. et al. Cloning of Dirac fermions in graphene superlattices. *Nature* **497**, 594–597 (2013).
9. Dean, C. et al. Hofstadter’s butterfly and the fractal quantum Hall effect in moiré superlattices. *Nature* **497**, 598–602 (2013).
10. Hunt, B. et al. Massive Dirac fermions and Hofstadter butterfly in a van der Waals heterostructure. *Science* **340**, 1427 (2013).
11. Cao, Y. et al. Correlated insulator behavior at half-filling in magic-angle graphene superlattices. *Nature* **556**, 80–84 (2018).
12. Cao, Y. et al. Unconventional superconductivity in magic-angle graphene superlattices. *Nature* **556**, 43–50 (2018).
13. Sharpe, A. et al. Emergent ferromagnetism near three-quarters filling in twisted bilayer graphene. *Science* **365**, 605 (2019).
14. Serlinc, M. et al. Intrinsic quantized anomalous Hall effect in a moiré heterostructure. *Science* **367**, 900-903 (2019).
15. Chen, G. et al. Signatures of tunable superconductivity in a trilayer graphene moiré

- superlattice. *Nature* **572**, 215–219 (2019).
16. Chen, G. et al. Evidence of a gate-tunable Mott insulator in a trilayer graphene moiré superlattice. *Nat. Phys.* **15**, 237–241 (2019).
 17. Chen, G. et al. Tunable correlated Chern insulator and ferromagnetism in a moiré superlattice. *Nature* **579**, 56–61 (2020).
 18. Wang, L. et al. New generation of moiré superlattices in doubly aligned hBN/graphene/hBN heterostructures. *Nano Lett.* **19**, 2371–2376 (2019).
 19. Wang, Z. et al. Composite super-moiré lattices in double-aligned graphene heterostructures. *Sci. Adv.* **5**, eaay8897 (2019).
 20. Finney, N. R. et al. Tunable crystal symmetry in graphene-boron nitride heterostructures with coexisting moiré superlattices. *Nat. Nanotechnol.* **14**, 1029 (2019).
 21. Yang, Y. et al. In situ manipulation of van der waals heterostructures for twistronics. *Sci. Adv.* **6**, eabd3655 (2020).
 22. Kuiru, M. et al. Enhanced electron-phonon coupling in doubly aligned hexagonal boron nitride bilayer graphene heterostructure. *Phys. Rev. B.* **103**, 115419 (2021).
 23. Anelković, M., Milovanović, S. P., Covaci, L., Peeters, F. M. Double moiré with a twist: Supermoiré in encapsulated graphene. *Nano Lett.* **20**, 979 (2020).
 24. Sun, X. et al. Correlated states in doubly aligned hBN/graphene/hBN heterostructures. *Nat Commun* **12**, 7196 (2021).
 25. Lu, X. et al. Superconductors, orbital magnets, and correlated states in magic-angle bilayer graphene. *Nature* **574**, 653–657 (2019).
 26. Zheng, Z. et al. Unconventional ferroelectricity in moiré heterostructures. *Nature* **588**, 71–76 (2020).
 27. Mao, J. et al. Evidence of flat bands and correlated states in buckled graphene superlattices. *Nature* **584**, 215–220 (2020).
 28. Xu, Y. et al. Creation of moiré bands in a monolayer semiconductor by spatially periodic dielectric screening. *Nat. Mater.* **20**, 645–649 (2021).
 29. Berdyugin, A. I. et al. Out-of-equilibrium criticalities in graphene superlattices. *Science* **375**, 430–433 (2022).

30. He, P. et al. Graphene moiré superlattices with giant quantum nonlinearity of chiral Bloch electrons. *Nat. Nanotechnol.* **17**, 378–383 (2022).
31. Woods, C. et al. Macroscopic self-reorientation of interacting two-dimensional crystals. *Nat Commun* **7**, 10800 (2016).
32. Wang, D. M. et al. Thermally induced graphene rotation on hexagonal boron nitride. *Phys. Rev. Lett.* **116**, 126101 (2016).
33. Eckmann, A. et al. Raman fingerprint of aligned graphene/hBN superlattices. *Nano Lett.* **13**, 5242–5246 (2013).
34. Xue, J. et al. Scanning tunnelling microscopy and spectroscopy of ultra-flat graphene on hexagonal boron nitride. *Nature Mater* **10**, 282–285 (2011).
35. Yankowitz, M. et al. Emergence of superlattice Dirac points in graphene on hexagonal boron nitride. *Nature Phys* **8**, 382–386 (2012).
36. Ahn, S. J. et al. Dirac electrons in a dodecagonal graphene quasicrystal. *Science* **361**, 782–786 (2018).
37. Pezzini, S. et al. 30°-twisted bilayer graphene quasicrystals from chemical vapor deposition. *Nano Lett.* **20**, 3313–3319 (2020).
38. Hu, J. X. et al. Room-temperature colossal magnetoresistance in terraced single-layer graphene. *Adv. Mater.* **32**, 37 2002201 (2020).
39. Hu, J. X. et al. Direct determination of spin-splitting energy in magnetic graphene by Landau fan shifts. Preprint at <https://doi.org/10.48550/arXiv.2205.11042> (2022).
40. Xu, Y. et al. Correlated insulating states at fractional fillings of moiré superlattices. *Nature* **587**, 214–218 (2020).
41. Shimazaki, Y. et al. Strongly correlated electrons and hybrid excitons in a moiré heterostructure. *Nature* **580**, 472–477 (2020).
42. Regan, E. C. et al. Mott and generalized Wigner crystal states in WSe₂/WS₂ moiré superlattices. *Nature* **579**, 359–363 (2020).
43. Jin, C. et al. Observation of moiré excitons in WSe₂/WS₂ heterostructure superlattices. *Nature* **567**, 76–80 (2019).

Acknowledgements

This work is supported by the Ministry of Education (MOE) Singapore under the Academic Research Fund Tier 2 (Grant No. MOE-T2EP50120-0015), by the Agency for Science, Technology and Research (A*STAR) under its Advanced Manufacturing and Engineering (AME) Individual Research Grant (IRG) (Grant No. A2083c0054), and by the National Research Foundation (NRF) of Singapore under its NRF-ISF joint program (Grant No. NRF2020-NRF-ISF004-3518). K.W. and T.T. acknowledge support from the JSPS KAKENHI (Grant Numbers 19H05790, 20H00354 and 21H05233).

Author contributions

A.A. conceived and supervised the project. J.X.H. designed and performed the experiments. J.Y.T. developed 30°-rotation alignment techniques and provided support and training on device fabrication process. M.M.A.E and U.C. carried out theoretical calculations under the supervision of S.A. Y.T.Z., J.Y.C., R.T. and J.B.L. helped to prepare sample and make the device. Z.H.W. helped the data analysis and interpretation. T.T. and K.W. provided the bulk hBN crystals. J.G. helped STM measurement under the supervision of A.T.S.W. J.X.H. and A. A. analyzed the experimental data and wrote the manuscript. All authors discussed the results and commented on the manuscript.

Competing interests

The authors declare no competing interests.

Additional information

Supplementary information is available for this paper at.

Reprints and permissions information is available at.

Correspondence should be addressed to A. Ariando.

Publisher's note: Springer Nature remains neutral with regard to jurisdictional claims in published maps and institutional affiliations.

Data availability. The data that support the plots within this paper and other findings of this study are available from the corresponding authors upon reasonable request.